nature materials

Article

https://doi.org/10.1038/s41563-024-01862-8

Uncovering the predictive pathways of lithium and sodium interchange in layered oxides

Received: 1 December 2022

Accepted: 14 March 2024

Published online: 16 April 2024

Check for updates

Yu Han[1], Weihang Xie[2], Grant T. Hill[1], Paul Smeets[3,4], Xiaobing Hu[3,4], Gangbin Yan[1], Siqi Zou[1], Jiadong Liu[1], Ronghui Wu[1], Fengyuan Shi[5], Hua Zhou[6], Pieremanuele Canepa[7,8] & Chong Liu[1]

Ion exchange is a powerful method to access metastable materials with advanced functionalities for energy storage applications. However, high concentrations and unfavourably large excesses of lithium are always used for synthesizing lithium cathodes from parent sodium material, and the reaction pathways remain elusive. Here, using layered oxides as model materials, we demonstrate that vacancy level and its corresponding lithium preference are critical in determining the accessible and inaccessible ion exchange pathways. Taking advantage of the strong lithium preference at the right vacancy level, we establish predictive compositional and structural evolution at extremely dilute and low excess lithium based on the phase equilibrium between $Li_{0.94}CoO_2$ and $Na_{0.48}CoO_2$. Such phase separation behaviour is general in both surface reaction-limited and diffusion-limited exchange conditions and is accomplished with the charge redistribution on transition metals. Guided by this understanding, we demonstrate the synthesis of Na_yCoO_2 from the parent Li_xCoO_2 and the synthesis of $Li_{0.94}CoO_2$ from Na_yCoO_2 at 1–1,000 Li/Na (molar ratio) with an electrochemical assisted ion exchange method by mitigating the kinetic barriers. Our study opens new opportunities for ion exchange in predictive synthesis and separation applications.

Ion exchange, that is, varying chemical composition while maintaining a solid framework, is one of the most important reactions in solid state chemistry. It is effective in broadening the library of metastable materials with distinct physical and chemical properties[1–3]. Ion exchange has achieved success in various fields, including nanocrystal synthesis to achieve quantum ionic solids with a variety of optical and electronic properties[4–6] and mineral utilization to determine the rheological and mechanical properties of soil and the fates of solutes[7,8]. Especially in the field of energy storage, ion exchange is applied to prepare novel lithium cathode materials with phases and properties that cannot be achieved via solid state synthesis such as O2-$LiCoO_2$ (refs. 9–12) (following Delmas et al.'s nomenclature, O as octahedral, classified by environments of inserted alkali atoms, and the other two types are tetrahedral (T) and prismatic (P), where the following number refers

[1]Pritzker School of Molecular Engineering, University of Chicago, Chicago, IL, USA. [2]Department of Materials Science and Engineering, National University of Singapore, Singapore, Singapore. [3]Department of Materials Science and Engineering, Northwestern University, Evanston, IL, USA. [4]The NUANCE Center, Northwestern University, Evanston, IL, USA. [5]Electron Microscopy Core, Research Resources Center, University of Illinois Chicago, Chicago, IL, USA. [6]X-ray Science Division, Advanced Photon Source, Argonne National Laboratory, Lemont, IL, USA. [7]Department of Electrical and Computer Engineering, University of Houston, Houston, TX, USA. [8]Texas Center for Superconductivity at the University of Houston, Houston, TX, USA. e-mail: chongliu@uchicago.edu

to the repeat unit number)[13], layered $LiMnO_2$ (refs. 14,15), A-$Li_{2/3}MO_2$ (A = O2, T2 (T as tetrahedral), O6, where M represents combinations among Li, Co, Mg, Mn, Ni and Ti)[16–22], $LiNi_{0.5}Mn_{0.5}O_2$ with reduced Ni/Li exchanges[23], alluaudite $LiMPO_4$ (M = Fe, Mn)[24,25] and multi-Li polyanionic cathode $Li_xNa_{1.5-x}VOPO_4F_{0.5}$ (ref. 2).

Despite all the successful examples, the Li and Na ion exchange mechanisms and pathways for cathode synthesis remain elusive. The exchange of structural Na in layered oxides by solution Li was proposed to initiate from the nucleation of a Li layer via slab gliding followed by layer-by-layer growth[11,12]. However, the relevant dimensions of the proposed physical processes, the corresponding composition (cation and vacancy level) changes and the spatial elemental distributions are unknown. Moreover, the reverse reaction to obtain metastable Na layered oxides from the parent Li layered oxides has not been reported before. Currently, ion exchange reactions are largely performed by the Edisonian approach and are resource intensive. Elevated temperature[1], high concentrations and large excesses of precursor ions (for example, ~5–10 total Li/Na ratio for Li cathode synthesis) were used as primary strategies to overcome all the kinetic barriers[10–12,14–25]. There is a lack of prediction capability to control the evolution pathways of both compositions and phases during ion exchange.

In this Article, to fill in the knowledge gap, we report predictive ion exchange and reveal the mechanism of Li and Na ion exchange in layered oxides using cobalt oxides as models. Counterintuitively, using Li ions of extremely low ratio (for example, 1–1,000 Li/Na molar ratio) and small excess (for example, 18% excess of Li to target amount), we can achieve near equilibrium exchange with Na_yCoO_2 by taking advantage of structural Li preference. Instead of forming Li_xCoO_2 with the same cation content ($x = y$), the structure nucleates a $Li_{0.94}CoO_2$ phase that has the smallest potential difference with the Na phase, which drives the Na phase change to form the equilibrium between $Na_{0.48}CoO_2$ and $Li_{0.94}CoO_2$. The phase separation and equilibrium behaviours allow us to predict not only the final compositions and phases but also the intermediate states to map out the kinetic pathways. The phase separation behaviour was also captured at far-from-equilibrium conditions with high Li concentrations and large Li excesses. We demonstrate that $Li_{0.94}CoO_2$ nucleation is a critical step during the ion exchange, following which the reaction proceeds with either a diffusion-limited (high Li ratio) or a surface reaction-limited (low Li ratio) mechanism. Additionally, we identify a large kinetic energy barrier at low vacancy levels that categorize the ion exchange pathways as accessible and inaccessible (unable to reach equilibrium). Guided by the understanding in vacancy-dependent ion preference and diffusion barriers, we realize Na_yCoO_2 (~98% Na purity) conversion from the parent Li_xCoO_2 and Na_yCoO_2 conversion to $Li_{0.94}CoO_2$ (~98% Li purity from 1–1,000 Li/Na molar ratio) via electrochemically assisted ion exchange, with the latter one of importance for Li extraction.

$Na_{0.48}CoO_2$ and $Li_{0.94}CoO_2$ phase equilibrium

For layered oxide, Li usually only takes the octahedral (O) site, while Na can also take the prismatic (P) site[26]. Transformation between O3 and P3 (and O2 and P2) can be readily realized by gliding MO_2 layers instead of breaking stacking sequence within individual MO_2 layers[27]. Figure 1a shows the galvanostatic curves (versus Na^+/Na) of O3-Li_xCoO_2 and P3-Na_yCoO_2 at slow kinetics (C/80), which represent mostly their thermodynamic differences. O3-Li_xCoO_2 and P3-Na_yCoO_2 have distinct phase transformations with respect to vacancy change. Importantly, the large voltage differences (ΔV) between Li_xCoO_2 and Na_yCoO_2 at the same vacancy (for example, ~1.0 V at $x = y = 0.67$) indicate the preference of the cobalt oxide framework for Li. The framework has larger Li preference at lower vacancy levels.

Platelet-like P3-$Na_{0.67}CoO_2$ particles (Supplementary Fig. 1) were used as model materials to systematically explore the ion exchange process. Na_yCoO_2 with varying y values (y = 0.37, 0.47, 0.57, 0.67, 0.77 and 0.87) were prepared by the electrochemical method (Methods). To control the ion exchange and limit possible kinetic pathways, we designed the ion exchange reaction near equilibrium using a low Li ratio (1–1,000 Li/Na molar ratio, 1 mM Li and 1 M Na mixed acetonitrile (ACN) solution unless specified). The open-circuit voltage (OCV; in a three-electrode system) of P3-Na_yCoO_2 during ion exchange was monitored. Interestingly, the shape of the OCV curve when using $Na_{0.67}CoO_2$ as the starting state is similar to the galvanostatic curve of Na_yCoO_2 in the range between $y = 0.67$ and $y = 0.48$ but with an additional final plateau at the voltage of 3.45 V (Fig. 1b). Four intermediate plateaus (I, II, III and IV) at 2.87 V, 3.10 V, 3.19 V and 3.25 V on the galvanostatic curve (Fig. 1a and Supplementary Fig. 2) also appear on the OCV curve of $Na_{0.67}CoO_2$ (Fig. 1b, inset), which indicates a similar phase transformation as charging. This 'pseudo-charging' behaviour (where the potential changes similarly to charging but without redox reactions) suggests that ion exchange with Li can induce a structure change of the starting Na_yCoO_2. 'Pseudo-charging' is also observed for the starting state of $Na_{0.57}CoO_2$. However, for other starting Na_yCoO_2 materials (y = 0.37, 0.47, 0.77 and 0.87), no 'pseudo-charging' behaviour was observed.

Synchrotron X-ray diffraction (XRD) analysis was conducted to identify the Li and Na phases after ion exchange. For parent Na_yCoO_2 before ion exchange, the (003) peaks gradually left shifted as the sodium content y decreased, corresponding to an expansion of interlayer distance (Fig. 1c). After ion exchange, unlike forming the intermediate phase with emerging diffraction peak located between Na (003) and Li (003) peaks observed at the elevated temperature[1], a new Li phase appeared for the cases with $Na_{0.57}CoO_2$ and $Na_{0.67}CoO_2$ as the starting states. The (003) peaks of the new Li phase for both cases were at the same position and assigned to $Li_{0.94}CoO_2$. Accompanied by the Li phase appearance, the Na (003) peaks of the $Na_{0.57}CoO_2$ and $Na_{0.67}CoO_2$, left shifted to the position of the $Na_{0.48}CoO_2$ phase (see Methods for $Li_{0.94}CoO_2$ and $Na_{0.48}CoO_2$ phase assignment). The continuation of the final plateau (Fig. 1b) and the corresponding constant chemical composition (Supplementary Fig. 3) indicate that the ion exchange process already reaches a steady state. More importantly, the formed $Li_{0.94}CoO_2$ phase and $Na_{0.48}CoO_2$ phase have the same open circuit voltage in the 1–1,000 Li/Na molar ratio solution, indicating that these two phases have the same electrochemical potential of electrons and are in equilibrium under this condition. However, for $Na_{0.37}CoO_2$ and $Na_{0.87}CoO_2$, no obvious Li phase was observed after 24 h ion exchange based on synchrotron XRD characterization.

Since two-phase equilibrium between $Li_{0.94}CoO_2$ and $Na_{0.48}CoO_2$ exists in the ion exchange process, we can calculate the total Li and Na contents a and b in the two-phase mixture (phase $Li_{0.94}CoO_2$ and phase $Na_{0.48}CoO_2$) having an overall composition of $Li_aNa_bCoO_2$ based on the vacancy level (see equilibrium equations in Methods). For the starting materials $Na_{0.72}CoO_2$, $Na_{0.67}CoO_2$ and $Na_{0.57}CoO_2$, the chemical compositions after ion exchange are calculated as $Li_{0.49}Na_{0.23}CoO_2$, $Li_{0.39}Na_{0.28}CoO_2$ and $Li_{0.18}Na_{0.39}CoO_2$ based on two-phase equilibrium and measured as $Li_{0.47}Na_{0.25}CoO_2$, $Li_{0.39}Na_{0.28}CoO_2$ and $Li_{0.21}Na_{0.36}CoO_2$ by inductively coupled plasma mass spectrometry (ICP-MS). The excellent agreement between the measured chemical compositions and predicted chemical compositions based on the equilibrium equation confirms the two-phase equilibrium between $Li_{0.94}CoO_2$ and $Na_{0.48}CoO_2$ (Fig. 1d). This is also supported by Rietveld refinement results (Fig. 1e and Supplementary Table 1). However, based on the two-phase equilibrium calculation, $Na_{0.77}CoO_2$ and $Na_{0.87}CoO_2$ should convert to $Li_{0.59}Na_{0.18}CoO_2$ and $Li_{0.80}Na_{0.07}CoO_2$, respectively. The experiment results showed that the final compositions ($Li_{0.21}Na_{0.56}CoO_2$ and $Li_{0.07}Na_{0.80}CoO_2$, respectively) had much less Li than the predicted value, indicating kinetic limitations. Such a kinetic barrier is extremely high; even after 15 days of ion exchange, the Li content a was still 0.17 instead of the predicted 0.90 for $Na_{0.92}CoO_2$, and even when we changed the exchange solution to 1 M Li, the ion exchange could not fully complete (Supplementary Fig. 4). A large kinetic barrier can be expected partially due to the vastly different diffusion coefficient (approximately two

https://doi.org/10.1038/s41563-024-01862-8

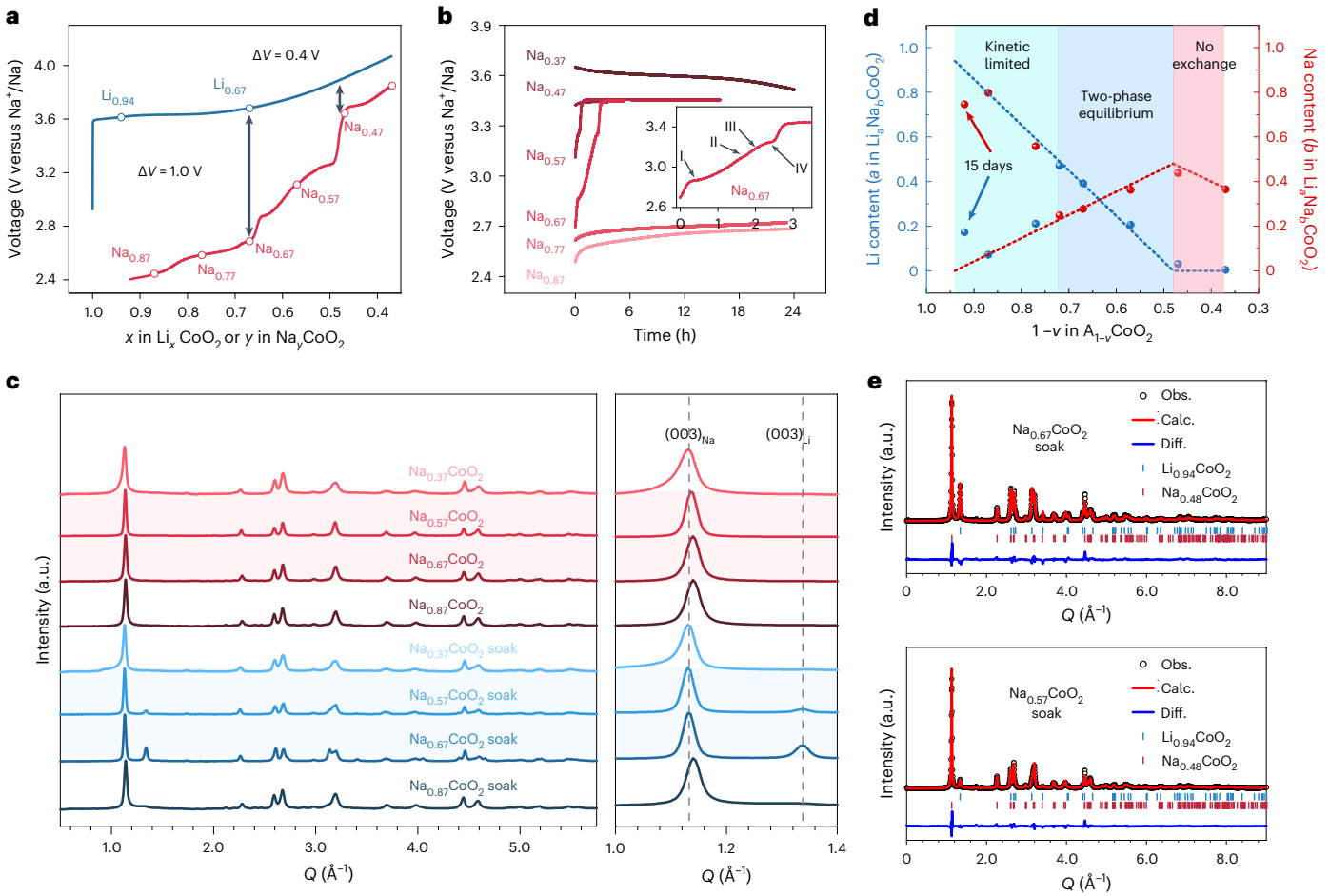

Fig. 1 | Phase separation and two-phase equilibrium between $Li_{0.94}CoO_2$ and $Na_{0.48}CoO_2$. **a**, Galvanostatic curves of P3-Na_yCoO_2 in the range of $0.37 < y < 0.92$ and Li_xCoO_2 in the range of $0.37 < x < 1.0$ at C/80. **b**, OCV curves of P3-Na_yCoO_2 ($y = 0.37, 0.47, 0.57, 0.67, 0.77$ and 0.87) during ion exchange. Inset: enlarged OCV curve of $Na_{0.67}CoO_2$ showing the 'pseudo-charging' behaviour with four characteristic plateaus. **c**, Synchrotron XRD patterns of Na_yCoO_2 ($y = 0.37, 0.57, 0.67$ and 0.87) before and after 24 h ion exchange. Dashed grey lines indicate the (003) peak positions of equilibrated phases $Na_{0.48}CoO_2$ (left) and $Li_{0.94}CoO_2$ (right). $Na_{0.57}CoO_2$ and $Na_{0.67}CoO_2$ that show phase equilibrium behaviours are highlighted. Scattering vector Q is used as the x axis. **d**, The Li content a and Na content b in the two-phase mixture of $Li_aNa_bCoO_2$ (overall composition) after exchange from starting material $A_{1-v}CoO_2$ as a function of vacancy level v (A = Li, Na or combination of Li and Na, $a + b = 1 - v$). The blue dots and red dots indicate the Li contents and Na contents measured after ion exchange of 24 h and 15 days (labelled by the arrows), for Na_yCoO_2 ($y = 0.37, 0.47, 0.57, 0.67, 0.72, 0.77$ and 0.87). The dashed lines are predicted Li and Na contents based on phase equilibrium. **e**, Rietveld refinements of patterns in **c**. $Na_{0.67}CoO_2$ (top) after 24 h ion exchange with 39.7% $Li_{0.94}CoO_2$ and 60.3% $Na_{0.48}CoO_2$ and $Na_{0.57}CoO_2$ (bottom) after 24 h ion exchange with 17.9% $Li_{0.94}CoO_2$ and 82.1% $Na_{0.48}CoO_2$. Obs., observation; Calc., calculation; Diff., difference between the observation and the calculation.

orders of magnitude) from the ~30% to ~10% vacancy level[28–31]. In the following section, we will demonstrate that this kinetic limitation can be overcome via an electrochemically assisted ion exchange process.

Based on the final compositions and phases, we divided the ion exchange process into three different regions. First, in the range of $0.48 \le a + b \le 0.72$ (Fig. 1d), two-phase equilibrium is established between $Li_{0.94}CoO_2$ and $Na_{0.48}CoO_2$. Second, with $0.72 < a + b \le 0.94$ (Fig. 1d), even though two-phase equilibrium is predicted, the ion exchange cannot complete due to large kinetic barriers at low vacancy levels[32–34]. Third, for $0.37 \le a + b < 0.48$ (Fig. 1d), no 'pseudo-charging' behaviour was observed and Na_yCoO_2 is the stable phase without ion exchange (confirmed by ICP-MS). As indicated by the potentials in Fig. 1a, with y in Na_yCoO_2 decreasing to 0.48, the cobalt oxide framework preference for Li decreased substantially (ΔV decreases from 1.0 V to 0.4 V). Therefore, for low starting Li ratio (1–1,000 Li/Na molar ratio), the driving force is insufficient to initiate the ion exchange. By using a higher Li ratio (1 M Li), the ion exchange of $Na_{0.37}CoO_2$ to the corresponding Li host is complete, confirming that the limitation is from the thermodynamic driving force (Supplementary Fig. 5). However, such ion exchange does not follow the two-phase equilibrium route between $Li_{0.94}CoO_2$ and $Na_{0.48}CoO_2$, since the cation content is out of the equilibrium range.

This phase separation and equilibrium phenomenon accompanied by the 'pseudo-charging' behaviour exist not only in the P3-Na_yCoO_2 system. We also observed similar phenomena for P2-Na_yCoO_2 exchanged with Li in 1–1,000 Li/Na molar ratio ACN (Supplementary Fig. 6). Based on the same characterization, the equilibrated Li phase and Na phase in the P2-Na_yCoO_2 system were assigned as O2-$Li_{0.94}CoO_2$ and P2-$Na_{0.46}CoO_2$, respectively.

Resolving ion exchange pathways

Before resolving ion exchange pathways, we need to understand the phase equilibrium between $Li_{0.94}CoO_2$ and $Na_{0.48}CoO_2$. From the galvanostatic curves (Fig. 1a), $Li_{0.94}CoO_2$ and $Na_{0.48}CoO_2$ have similar potentials that allow the structure to establish equilibrium. In contrast, direct conversion from $Na_{0.67}CoO_2$ to $Li_{0.67}CoO_2$ is not thermodynamically favourable due to the large potential differences shown in Fig. 1a. Moreover, the phase equilibrium between $Li_{0.94}CoO_2$ and $Na_{0.48}CoO_2$

https://doi.org/10.1038/s41563-024-01862-8

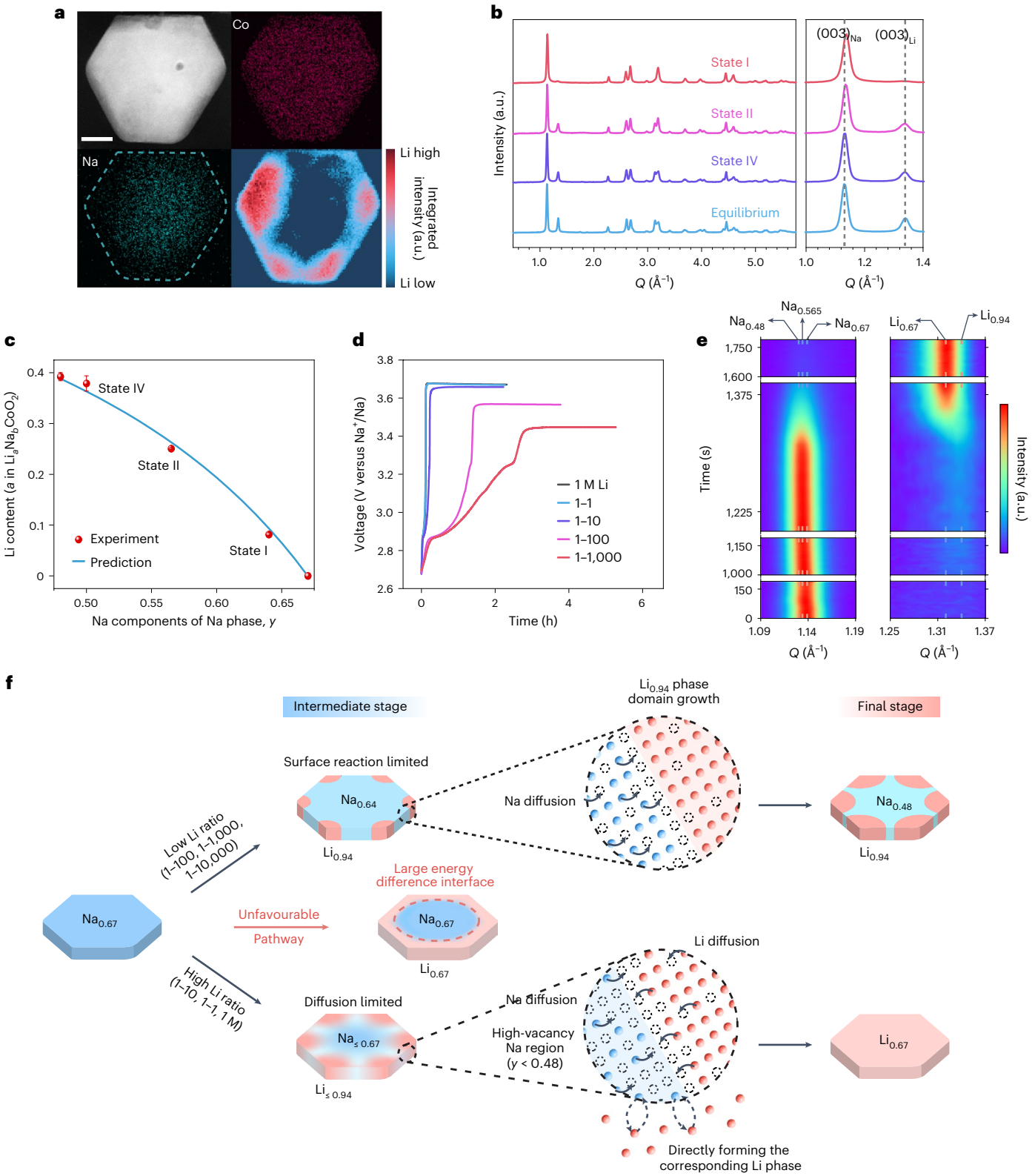

Fig. 2 | Revealing structural evolution during Li ion exchange with $Na_{0.67}CoO_2$. **a**, HAADF-STEM image, EDS maps and Li EELS map of $Na_{0.67}CoO_2$ after reaching equilibrium. Na locates in the centre and Li locates at the edges and corners of the particle. Scale bar, 30 nm. The Li signal is extracted between the energy range of 60.3 eV and 62.8 eV (Supplementary Fig. 7). **b**, Synchrotron XRD patterns of different intermediate states. Dashed grey lines indicate the (003) peak positions of equilibrated phases $Na_{0.48}CoO_2$ (left) and $Li_{0.94}CoO_2$ (right). Scattering vector Q is used as the x axis. **c**, Lithium contents as measured (red dots) and as calculated based on the evolution equation (blue line) as a function of the Na phase during ion exchange. Each point represents the mean ± s.d. from three independent experiments. **d**, OCV curves of $Na_{0.67}CoO_2$ ion exchanging in ACN solutions with different Li/Na ratios. The curve of 1 M Li (black line) is overlapping with the curve of 1–1 Li/Na (blue line). **e**, In situ synchrotron XRD patterns of Na (003) peak and Li (003) peak during $Na_{0.67}CoO_2$ ion exchange in 1 M Li ACN solution. The nucleation and left shift of the $Li_{0.94}CoO_2$ peak starting from ~1,000 s accompanied by a Na (003) peak left shift were clearly revealed. **f**, A schematic showing both the surface reaction-limited and the diffusion-limited exchange pathways for in-plane phase evolution at low Li and high Li ratios, respectively. $Na_{0.64}CoO_2$ is one example of Na phases in the surface reaction-limited ion exchange pathway.

indicates that charge redistribution between Co^{3+}/Co^{4+} must occur during the phase change. The in-plane electron resistivity is much lower than that of out-of-plane[35] and across-particle. Therefore, in-layer intra-particle phase separation would be the most feasible pathway to establish the phase equilibrium. We then performed scanning transmission electron microscopy (STEM) energy-dispersive X-ray spectroscopy and electron energy loss spectroscopy (EELS) to resolve the Na and Li distribution, respectively. The elemental mapping shows Na mainly in the centre and Li at the corners and edges in a single hexagonal-like particle (Fig. 2a and Supplementary Fig. 7). This result indicates the coexistence of Li and Na in the same layer and supports the in-layer intra-particle phase separation, even though Li and Na are commonly thought to not coexist in one layer[20]. Additionally, various interlayer spacings throughout a single layer were observed (Supplementary Fig. 8), which indicates that the ion exchange process does not follow the slab-by-slab exchange route[11,12,36]. Density functional theory (DFT) calculation was conducted to better understand the phase separation. For modelling convenience, $Li_{0.94}CoO_2$ and $Na_{0.48}CoO_2$ were modelled as $Li_{1.0}CoO_2$ and $Na_{0.5}CoO_2$, respectively. The interfacial energy at the interface between $Li_{1.0}CoO_2$ and $Na_{0.5}CoO_2$ is 0.8 J m^{-2}, which is slightly higher than the interfacial energy at the interface between $Li_{0.67}CoO_2$ and $Na_{0.67}CoO_2$ (0.5 J m^{-2}; Supplementary Fig. 9). This may be attributed to the mechanical strain energy caused by larger interlayer distance difference between $Li_{1.0}CoO_2$ and $Na_{0.5}CoO_2$ compared with $Li_{0.67}CoO_2$ and $Na_{0.67}CoO_2$. Therefore, phase separation into $Li_{0.94}CoO_2$ and $Na_{0.48}CoO_2$ is mainly controlled by thermodynamics, as evidenced by the coexistence between $Li_{1.0}CoO_2$ and $Na_{0.5}CoO_2$ in the ternary phase diagram (Supplementary Fig. 10) and the similar electrochemical potential between $Li_{0.94}CoO_2$ and $Na_{0.48}CoO_2$ shown in the galvanostatic curves (Fig. 1a). The Li–Na mixing is thermodynamically unfavourable, and the decomposition energy from $Li_{0.33}Na_{0.33}CoO_2$ (mixing phase) into $Li_{1.0}CoO_2$–$Na_{0.5}CoO_2$ is 23 meV per atom.

To gain a full picture of the ion exchange pathways, several intermediate states during ion exchange were characterized by synchrotron XRD. The ion exchange process of $Na_{0.67}CoO_2$ was quenched at the I, II and IV plateaus, being denoted as state I, II and IV, respectively. At state I, the $Li_{0.94}CoO_2$ structure was detected (Fig. 2b) instead of $Li_{0.67}CoO_2$ as proposed in the slab gliding model[12]. The formation of $Li_{0.94}CoO_2$ is favourable since it has the smallest potential difference to Na_yCoO_2 ($y > 0.48$). The (003) peaks of Na_yCoO_2 phase left shifted from state I to the final equilibrium. The observed phase transformation indicates that the ion exchange starts with $Li_{0.94}CoO_2$ nucleation, and then the Na phase changes from $Na_{0.67}CoO_2$ to the final equilibrated phase $Na_{0.48}CoO_2$ as $Li_{0.94}CoO_2$ phase grows. The persistence of $Li_{0.94}CoO_2$ phase during the entire ion exchange allows us to resolve the chemical composition and phase evolution of $Li_aNa_bCoO_2$ based on the coexistence of $Li_{0.94}CoO_2$ and Na_yCoO_2 (determined by OCV) phases (see the evolution equation in Methods). The chemical compositions calculated based on the evolution equation, ICP-MS measurement, and the Rietveld refinement all showed good agreement, supporting the proposed evolution pathway (Fig. 2c, Supplementary Fig. 11 and Supplementary Table 2).

To understand whether the proposed phase separation process is a general evolution pathway, we studied the ion exchange process of $Na_{0.67}CoO_2$ at different Li/Na molar ratios. As shown in Fig. 2d, all the OCV curves showed 'pseudo-charging' behaviour in 1–1,000, 1–100, 1–10, 1–1 Li/Na molar ratio (with fixed Na concentration of 1 M) and 1 M Li ACN solution, but with different plateaus numbers and final plateau potentials. The four intermediate plateaus during Na phase transformation were still visible in the 1–100 and 1–10 cases (Supplementary Fig. 12). For 1–1 and 1 M Li, the fast exchange kinetics makes capturing intermediate steps challenging, but the appearance of the first plateau (Supplementary Fig. 12) was observed. We then performed in situ synchrotron XRD for the case of 1 M Li. The emergence of the $Li_{0.94}CoO_2$ (003) peak at ~1,225–1,375 s (Fig. 2e) demonstrates again that ion exchange prefers to nucleate the $Li_{0.94}CoO_2$ phase. However, in this condition, both Li and Na phases changed after $Li_{0.94}CoO_2$ nucleation as shown by the left shift of both Li and Na peaks (Fig. 2e), and finally, a single $Li_{0.67}CoO_2$ phase was established with the disappearance of the Na phase (Supplementary Fig. 13). This complete exchange is reasonable since the driving force (Li concentration) is much larger, which is also shown in Supplementary Table 3 and Supplementary Fig. 5.

This result points to two ion exchange routes following $Li_{0.94}CoO_2$ nucleation (Fig. 2f). When the solution Li ratio is low (for example, 1–1,000 Li/Na molar ratio), the exchange of Li ion from the solution with surface Na is the rate-limiting step (surface reaction limited). Structural Na can diffuse to fill up the vacancy formed from $Li_{0.94}CoO_2$ phase nucleation and growth. Therefore, we only observed the Na phase change and a persistent $Li_{0.94}CoO_2$ phase in the whole exchange process. When the solution Li ratio is high (for example, 1 M Li), Li can quickly exchange with surface Na and nucleate a $Li_{0.94}CoO_2$ phase. The fast nucleation and growth of $Li_{0.94}CoO_2$ phase leave nearby domains with much higher vacancy levels. In this case, bulk Na diffusion alone cannot catch up with the ion exchange rate (diffusion limited) and the diffusion of both Li and Na occurs to avoid forming unstable domains. Additionally, as evidenced by Supplementary Fig. 5, high-vacancy Na phases (Na_yCoO_2, $y \leq 0.48$) can directly exchange with solution Li skipping the $Li_{0.94}CoO_2$ nucleation when the solution Li ratio is high (for example, 1 M Li). Hence, in the P3-Na_yCoO_2 in situ synchrotron XRD, we observed the left shift of Na peak caused by $Li_{0.94}CoO_2$ nucleation and growth, then the Li peak left shift to $Li_{0.67}CoO_2$ due to the merging of $Li_{0.94}CoO_2$ with high-vacancy Li domains (formed from the direct conversion of high-vacancy Na phases). The diffusion-limited ion exchange was also observed for P2-Na_yCoO_2 exchanging with 1 M Li. Due to the large particle size, both $Li_{0.94}CoO_2$ and high-vacancy Li_xCoO_2 ($x \leq 0.46$) were observed without merging accompanied by a high-vacancy Na_yCoO_2 ($y \leq 0.46$) phase (Supplementary Fig. 14).

Pure Na_yCoO_2 from Li_xCoO_2 via reversed ion exchange

Despite successful ion exchange to make Li cathodes from Na parent materials, the reversed ion exchange with solution Na replacing the structural Li to achieve pure Na_yCoO_2 has not been reported before. Initiating the process with a full Li structure without any vacancy only allows less than 1% of exchange at elevated temperature[37]. Here we demonstrated that a pure Na_yCoO_2 can be achieved from O3-Li_xCoO_2 when high structural Li preference regions are avoided. $Li_{0.40}CoO_2$, $Li_{0.50}CoO_2$ and $Li_{0.60}CoO_2$ were prepared (electrochemical deintercalation from the commercial $LiCoO_2$) for the demonstration. The OCV curves went through a series of slopes and plateaus indicating the occurrence of ion exchange (Fig. 3a). After reaching equilibrium, sample '$Li_{0.40}CoO_2$ soak' and '$Li_{0.50}CoO_2$ soak' only showed diffraction peaks from Na phase, whereas sample '$Li_{0.60}CoO_2$ soak' had both the diffraction peaks of $Li_{0.94}CoO_2$ and $Na_{0.48}CoO_2$ phases (Fig. 3b)[36]. The observed two phases ($Li_{0.94}CoO_2$ and $Na_{0.48}CoO_2$) at equilibrium via Na ion exchange with starting Li_xCoO_2 are the same two phases as we observed via Li ion exchange with starting Na_yCoO_2. The total Li (a) and Na (b) contents in the two-phase mixture $Li_aNa_bCoO_2$ were calculated. Li contents a are 0.01 (~98% Na purity), 0.05 and 0.24 confirmed by ICP-MS (Fig. 3c) for starting materials $Li_{0.40}CoO_2$, $Li_{0.50}CoO_2$ and $Li_{0.60}CoO_2$, which agree with the predicted compositions of $Na_{0.4}CoO_2$, $Li_{0.04}Na_{0.46}CoO_2$, and $Li_{0.25}Na_{0.35}CoO_2$, respectively, based on the phase equilibrium between $Li_{0.94}CoO_2$ and $Na_{0.48}CoO_2$. The exchanged $Na_{0.48}CoO_2$ from $Li_{0.48}CoO_2$ was used for further characterization. STEM imaging showed a 5.5 Å interlayer distance confirming the $Na_{0.48}CoO_2$ phase (Fig. 3d and Supplementary Fig. 15). The uniform distribution of Na EDS signal on both the particle ensemble level (scanning electron micrograpy (SEM); Fig. 3e) and the single particle level (STEM; Fig. 3f) indicates the completion of ion exchange between solution Na and structural Li. These results clearly indicate that the reverse exchange process is achievable and follows the two-phase equilibrium between $Li_{0.94}CoO_2$ and $Na_{0.48}CoO_2$.

https://doi.org/10.1038/s41563-024-01862-8

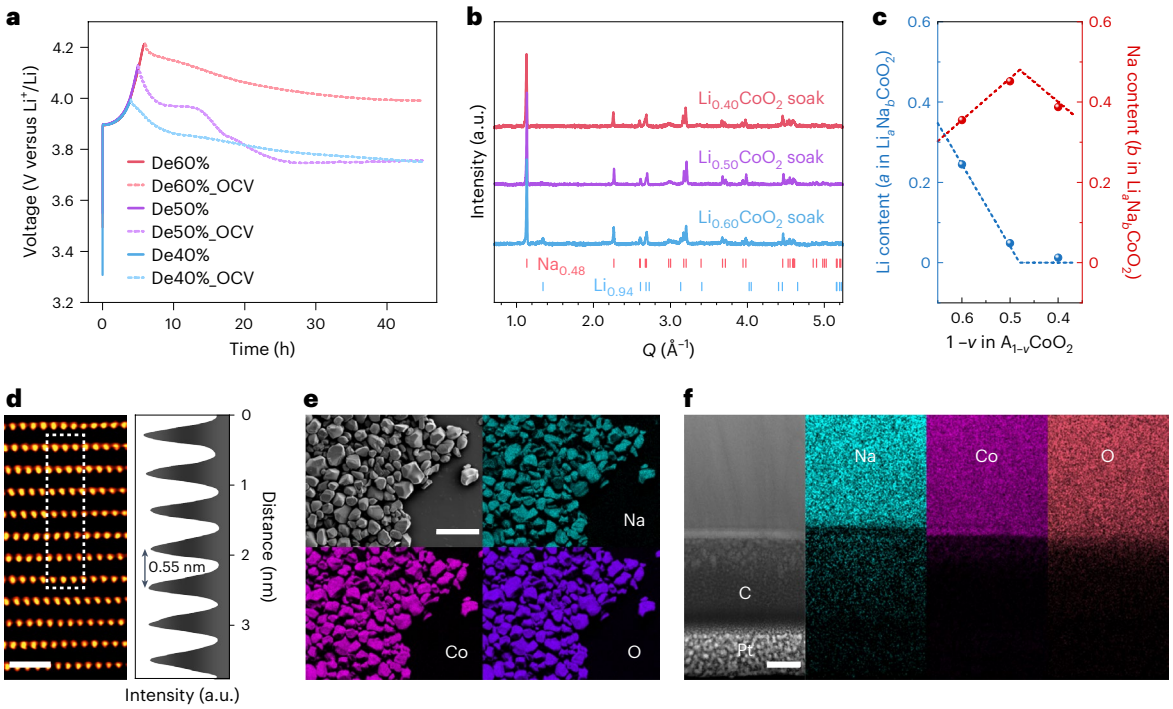

Fig. 3 | Reverse conversion from Li_xCoO_2 to Na_yCoO_2. a, Electrochemical curves of commercial $LiCoO_2$ after deintercalation of 40% (De40%), 50% (De50%) and 60% (De60%) capacities in 1–1,000 Li/Na molar ratio solution at C/10 with OCV curves for 41 h (De40%_OCV), 40 h (De50%_OCV) and 39 h (De60%_OCV) soaking, respectively. **b**,**c**, XRD patterns (**b**) and chemical compositions (**c**) of $Li_{0.40}CoO_2$, $Li_{0.50}CoO_2$ and $Li_{0.60}CoO_2$ after reaching equilibrium in 1 M Na solution. The dashed lines indicate predicted Li and Na contents based on phase equilibrium. Scattering vector Q is used as the x axis in **b**. v, vacancy level. **d**, An atomic resolution HAADF-STEM image of fully converted $Na_{0.48}CoO_2$ along the [010] zone axis and the signal profile from the dashed area. Scale bar, 1 nm. **e**, An SEM image and EDS maps of fully converted $Na_{0.48}CoO_2$. Scale bar, 30 µm. **f**, An HAADF-STEM image and EDS maps of fully converted $Na_{0.48}CoO_2$. Scale bar, 50 nm.

Electrochemically assisted ion exchange

Next, we demonstrate a strategy to mitigate the inaccessible ion exchange pathway caused by the large kinetic barrier and realize the formation of $Li_{0.94}CoO_2$ from $Na_{0.67}CoO_2$ at a low Li ratio (1–1,000 Li/Na molar ratio) and small Li excess (18% excess of Li to target amount; Methods). The two-phase equilibrium between $Li_{0.94}CoO_2$ and $Na_{0.48}CoO_2$ predicted a pure Li phase at $a + b \geq 0.94$. However, in the range of $0.72 < a + b < 0.94$, the final exchanged products did not follow the prediction (Fig. 1d). Inspired by the established structure evolution pathway, we design the ion exchange to start from $Na_{0.67}CoO_2$ phase with enough vacancies and increase the cation content $a + b$ to ~0.94 by multiple electrochemical intercalations and ion exchange to maintain $0.48 \leq y \leq 0.67$ in Na_yCoO_2 phase for fast ion exchange.

As shown in Fig. 4a, $Na_{0.67}CoO_2$ first went through the ion exchange process (first OCV). After the first phase equilibrium was established, the electrode was intercalated to the initial potential of $Na_{0.67}CoO_2$ (first inter) and allowed for ion exchange (second OCV) to restore the phase equilibrium where the potential went back to the equilibrium potential once we stopped the intercalation current. This process was repeated until the electrode reached its full capacity. Moreover, the intercalation voltage profile (Fig. 4a, inset) also shows the same four plateaus, which correspond to the transformation from $Na_{0.48}CoO_2$ to $Na_{0.67}CoO_2$. After three times of intercalation, the total amount of alkali-metal ions reaches 0.92 ($a + b = 0.92$ for $Li_aNa_bCoO_2$).

Even though the intercalation process is accompanied by a simultaneous ion exchange process (Supplementary Figs. 16 and 17a), the chemical composition evolution during the whole process can be predicted using coexistence of $Li_{0.94}CoO_2$ and Na_yCoO_2 phases (Fig. 4b). The Na phase was determined by the electrochemical potential (Supplementary Figs. 17b and 18). The compositions measured by ICP-MS and calculated on the basis of the evolution equation at intermediate steps (for example, progress points b, d, f, and h) show excellent matching (Fig. 4c). With the electrochemically assisted ion exchange, a complete exchanged lithium cobalt oxide ($Li_{0.90}Na_{0.02}CoO_2$, overall composition) is obtained. A minor 2% of Na, based on ICP-MS, is detected in the structure, which also exists for the ion exchange conducted with a high Li ratio and large excess ($Li_{0.95}Na_{0.016}CoO_2$ was obtained from exchange in 5 M LiOH and LiCl solution (1:1) for 19 h). The structural characterization shows pure XRD patterns of $Li_{0.94}CoO_2$ (Fig. 4d). The corresponding 4.7 Å interlayer spacing was also observed for $Li_{0.90}Na_{0.02}CoO_2$ by high-angle annular dark-field (HAADF)-STEM, which supports the successful conversion to $Li_{0.94}CoO_2$ (Fig. 4e and Supplementary Fig. 19). Compared with the incomplete exchange of $Na_{0.92}CoO_2$ ($Li_{0.17}Na_{0.75}CoO_2$) shown in Fig. 1d, this complete exchange to $Li_{0.90}Na_{0.20}CoO_2$ indicates that the Na component y in the Na_yCoO_2 phase plays an important role in determining the ion exchange pathways. However, the atomic-level picture regarding the dynamics of vacancy rearrangement during ion exchange still needs further investigation.

Since the $Na_{0.67}CoO_2$ to $Li_{0.94}CoO_2$ conversion was done in 1–1,000 Li/Na molar ratio solution, it marks the excellent structural selectivity (4.5×10^4; Methods) for layered oxide to enable Li extraction application with ~98% Li purity. Moreover, we demonstrated that the Li extraction can also be achieved using an even lower Li ratios (1–10,000 Li/Na molar ratio; Supplementary Fig. 20).

Finally, we labelled all the accessible conversion pathways for Li and Na ion exchange in layered cobalt oxide (Fig. 5). All the Li_xCoO_2 can be achieved from Li exchanging with Na_yCoO_2 given sufficient driving force and avoiding the kinetic-limited regions. However, only Na_yCoO_2 with $y \leq 0.48$ can be achieved at large Na concentrations and excesses, resulting from the extremely strong Li preference of the cobalt oxide framework. Our results indicate that the phase equilibrium between $Li_{0.94}CoO_2$ and $Na_{0.48}CoO_2$ plays a key role in determining the ion exchange pathway.

https://doi.org/10.1038/s41563-024-01862-8

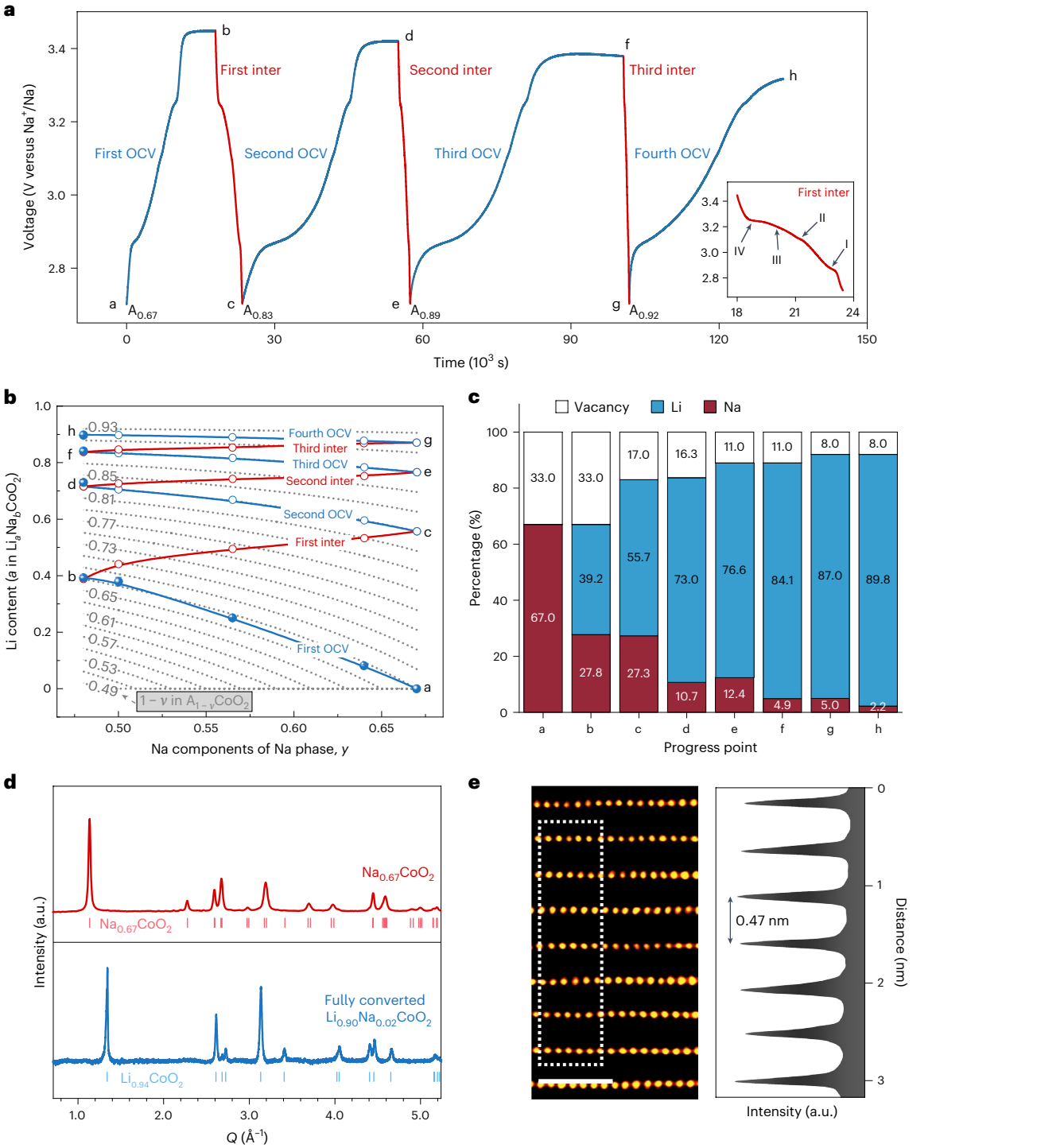

Fig. 4 | Full conversion from Na parent host to Li_xCoO_2 by electrochemically assisted ion exchange. a, Electrochemical curves of the electrochemically assisted ion exchange process. Once the intercalation (inter) current (C/10) stops, the OCV goes back to equilibrium voltage through Na phase change. Inset: enlarged first intercalation curve also shows the four characterized plateaus. **b**, Lithium contents (a) as a function of the Na phase (y in Na_yCoO_2) and the overall composition ($1-v$) during the electrochemically assisted ion exchange process. The solid balls indicate the measured composition via ICP-MS. Each point represents the mean ± s.d. from three independent experiments. The empty circles indicate the calculation based on the voltages and capacities in **a**. Dashed grey lines indicate the predicted ion exchange composition evolution based on the evolution equation. Parallel electrochemically assisted ion exchange experiments are conducted and stopped at state I (refers to $Na_{0.64}$), state II (refers to $Na_{0.565}$), state IV (refers to $Na_{0.50}$) and points b, d, f and h in **a**, respectively. The chemical compositions were measured by ICP-MS. **c**, The chemical compositions at different progress points shown in **b**. **d**, The XRD patterns of original P3-$Na_{0.67}CoO_2$ and fully converted $Li_{0.90}Na_{0.02}CoO_2$. Scattering vector Q is used as the x axis. **e**, An atomic resolution HAADF-STEM image of fully converted $Li_{0.90}Na_{0.02}CoO_2$ along the [010] zone axis and the signal profile from the dashed area. Scale bar, 1 nm.

The established prediction on the compositional and structural evolution based on the phase equilibrium between $Li_{x'}MO_2$ and $Na_{y'}MO_2$ is transferrable (M is transition metals; x' and y' are the cation contents of equilibrated Li and Na phases; $x' = 0.94$, and $y' = 0.48$ for the cobalt oxide system). We validated this in the O3-$Na_yNi_{0.5}Mn_{0.5}O_2$ and O3-$Na_yNi_{0.5}Mn_{0.3}Ti_{0.2}O_2$ systems in addition

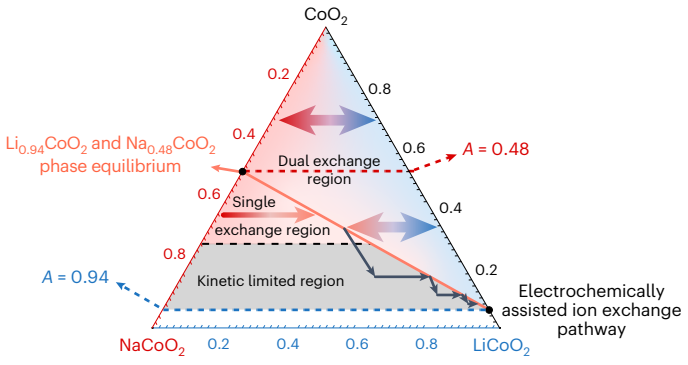

Fig. 5 | Phase diagram of Li and Na interchange in layered cobalt oxides. The two-phase equilibrium between $Li_{0.94}CoO_2$ and $Na_{0.48}CoO_2$ (orange line) divides the whole cation range into two different regions. In the region (dual exchange region) above the equilibrium line, dual ion exchange Li_xCoO_2–Na_yCoO_2 ($y = x$) or Li_xCoO_2–$Li_aNa_bCoO_2$ (equilibrium composition) can be achieved. In the region (single exchange region) below the equilibrium line, only Na_yCoO_2 exchanging with Li can be approached due to the strong structural Li preference. The kinetic barrier in this single exchange region is extremely large when the vacancy level is inadequate ($A > 0.72$, $A = a + b$ in $Li_aN_{ab}CoO_2$). The electrochemically assisted ion exchange pathway is highlighted with black arrows. The thickness of the colour arrow indicates the driving force of the targeted ion in solutions (for example, Na_yCoO_2 exchange with 1–1,000 Li/Na molar ratio and 1 M Li are shown by thin and thick arrows, respectively).

to the Na_yCoO_2 system discussed above (Supplementary Fig. 21). The strong oxide framework Li preference indicated by the large voltage difference between Li_xMO_2 and Na_yMO_2 ensures the occurrence of ion exchange in low Li ratio conditions. 'Pseudo-charging' behaviour is general in these Li/Na exchange systems (Supplementary Fig. 22). Distinct and aligned Li (003) and Na (003) peaks at different vacancy levels illustrate that the exchange at low Li ratio conditions in different transition metal layered oxide systems follows the proposed phase separation and equilibrium pathway, which is also evidenced by the consistence between the measured and the calculated chemical compositions.

In conclusion, we showed that the large thermodynamic Li preference of the cobalt oxide framework can trigger the exchange of Na_yCoO_2 at an extremely low Li ratio (for example, 1–10,000 Li/Na molar ratio) and small excess. In this work, we identify general ion exchange pathways whereby $Li_{0.94}CoO_2$ nucleates first; this is followed by a surface reaction-limited exchange pathway at near equilibrium conditions (for example, 1–1,000 Li/Na molar ratio) or a diffusion-limited exchange pathway far from the equilibrium conditions (for example, 1 M Li). Guided by the understanding of the ion exchange mechanism, Na_yCoO_2 conversion from the parent Li_xCoO_2 is demonstrated and Na_yCoO_2 conversion to $Li_{0.94}CoO_2$ is realized via electrochemically assisted ion exchange. The proposed ion exchange pathway can be extended to other transition metal layered oxide systems. Our work opens new opportunities for ion exchange in predictive synthesis and Li extraction.

Online content

Any methods, additional references, Nature Portfolio reporting summaries, source data, extended data, supplementary information, acknowledgements, peer review information; details of author contributions and competing interests; and statements of data and code availability are available at https://doi.org/10.1038/s41563-024-01862-8.

References

1. Gwon, H. et al. Ion-exchange mechanism of layered transition-metal oxides: case study of $LiNi_{0.5}Mn_{0.5}O_2$. *Inorg. Chem.* **53**, 8083–8087 (2014).
2. Park, Y.-U. et al. In situ tracking kinetic pathways of Li^+/Na^+ substitution during ion-exchange synthesis of $Li_xNa_{1.5-x}VOPO_4F_{0.5}$. *J. Am. Chem. Soc.* **139**, 12504–12516 (2017).
3. Kamysbayev, V. et al. Covalent surface modifications and superconductivity of two-dimensional metal carbide MXenes. *Science* **369**, 979–983 (2020).
4. Son, D. H., Hughes, S. M., Yin, Y. & Alivisatos, A. P. Cation exchange reactions in ionic nanocrystals. *Science* https://doi.org/10.1126/science.1103755 (2004).
5. Beberwyck, B. J. & Alivisatos, A. P. Ion exchange synthesis of III–V nanocrystals. *J. Am. Chem. Soc.* **134**, 19977–19980 (2012).
6. Li, Z., Saruyama, M., Asaka, T., Tatetsu, Y. & Teranishi, T. Determinants of crystal structure transformation of ionic nanocrystals in cation exchange reactions. *Science* **373**, 332–337 (2021).
7. Zou, Y.-C. et al. Ion exchange in atomically thin clays and micas. *Nat. Mater.* **20**, 1677–1682 (2021).
8. Whittaker, M. L., Lammers, L. N., Carrero, S., Gilbert, B. & Banfield, J. F. Ion exchange selectivity in clay is controlled by nanoscale chemical–mechanical coupling. *Proc. Natl Acad. Sci. USA* **116**, 22052–22057 (2019).
9. Delmas, C., Braconnier, J.-J. & Hagenmuller, P. A new variety of $LiCoO_2$ with an unusual oxygen packing obtained by exchange reaction. *Mater. Res. Bull.* **17**, 117–123 (1982).
10. Carlier, D. et al. On the metastable O_2-type $LiCoO_2$. *Solid State Ion.* **144**, 263–276 (2001).
11. Tournadre, F. et al. On the mechanism of the P2–$Na_{0.70}CoO_2$→O_2–$LiCoO_2$ exchange reaction—part I: proposition of a model to describe the P2–O2 transition. *J. Solid State Chem.* **177**, 2790–2802 (2004).
12. Tournadre, F., Croguennec, L., Willmann, P. & Delmas, C. On the mechanism of the P2–$Na_{0.70}CoO_2$→O_2–$LiCoO_2$ exchange reaction—part II: an in situ X-ray diffraction study. *J. Solid State Chem.* **177**, 2803–2809 (2004).
13. Delmas, C., Fouassier, C. & Hagenmuller, P. Structural classification and properties of the layered oxides. *Phys. B+C.* **99**, 81–85 (1980).
14. Capitaine, F., Gravereau, P. & Delmas, C. A new variety of $LiMnO_2$ with a layered structure. *Solid State Ion.* **89**, 197–202 (1996).
15. Armstrong, A. R. & Bruce, P. G. Synthesis of layered $LiMnO_2$ as an electrode for rechargeable lithium batteries. *Nature* **381**, 499–500 (1996).
16. Paulsen, J. M., Donaberger, R. A. & Dahn, J. R. Layered T2-, O6-, O2-, and P2-type A2/3[M'2+1/3M4+2/3]O_2 bronzes, A = Li, Na; M' = Ni, Mg; M = Mn, Ti. *Chem. Mater.* **12**, 2257–2267 (2000).
17. Paulsen, J. M. & Dahn, J. R. O_2-type $Li_{2/3}[Ni_{1/3}Mn_{2/3}]O_2$: a new layered cathode material for rechargeable lithium batteries ii. structure, composition, and properties. *J. Electrochem. Soc.* **147**, 2478 (2000).
18. Paulsen, J. M., Thomas, C. L. & Dahn, J. R. Layered Li-Mn-oxide with the O2 structure: a cathode material for Li-ion cells which does not convert to spinel. *J. Electrochem. Soc.* **146**, 3560–3565 (1999).
19. Paulsen, J. M. & Dahn, J. R. Studies of the layered manganese bronzes, $Na_{2/3}[Mn_{1-x}M_x]O_2$ with M=Co, Ni, Li, and $Li_{2/3}[Mn_{1-x}M_x]O_2$ prepared by ion-exchange. *Solid State Ion.* **126**, 3–24 (1999).
20. Paulsen, J. M., Larcher, D. & Dahn, J. R. O2 structure $Li_{2/3}[Ni_{1/3}Mn_{2/3}]O_2$: a new layered cathode material for rechargeable lithium batteries III. Ion exchange. *J. Electrochem. Soc.* **147**, 2862–2867 (2000).
21. Lu, Z., Donaberger, R. A., Thomas, C. L. & Dahn, J. R. T2 and O2 $Li_{2/3}[Co_xNi_{1/3-x/2}Mn_{2/3-x/2}]O_2$ electrode materials. *J. Electrochem. Soc.* **149**, A1083 (2002).
22. Lu, Z. & Dahn, J. R. The effect of Co substitution for Ni on the structure and electrochemical behavior of T2 and O2 structure $Li_{2/3}[Co_xNi_{1/3-x}Mn_{2/3}]O_2$. *J. Electrochem. Soc.* **148**, A237 (2001).

23. Kang, K., Meng, Y. S., Bréger, J., Grey, C. P. & Ceder, G. Electrodes with high power and high capacity for rechargeable lithium batteries. *Science* **311**, 977–980 (2006).
24. Kim, J. et al. Alluaudite $LiMnPO_4$: a new Mn-based positive electrode for Li rechargeable batteries. *J. Mater. Chem. A* **2**, 8632–8636 (2014).
25. Kim, J. et al. $LiFePO_4$ with an alluaudite crystal structure for lithium ion batteries. *Energy Environ. Sci.* **6**, 830–834 (2013).
26. Zhao, C. et al. Rational design of layered oxide materials for sodium-ion batteries. *Science* **370**, 708–711 (2020).
27. Radin, M. D., Alvarado, J., Meng, Y. S. & Van der Ven, A. Role of crystal symmetry in the reversibility of stacking-sequence changes in layered intercalation electrodes. *Nano Lett.* **17**, 7789–7795 (2017).
28. Xia, H., Meng, S. Y., Lu, L. & Ceder, G. Electrochemical behavior and Li diffusion study of $LiCoO_2$ thin film electrodes prepared by PLD. in *Advanced Materials for Micro- and Nano-Systems (AMMNS)* (2007); http://hdl.handle.net/1721.1/35827
29. Hess, A. et al. Determination of state of charge-dependent asymmetric Butler–Volmer kinetics for Li_xCoO_2 electrode using GITT measurements. *J. Power Sources* **299**, 156–161 (2015).
30. Shibata, T., Fukuzumi, Y., Kobayashi, W. & Moritomo, Y. Fast discharge process of layered cobalt oxides due to high Na^+ diffusion. *Sci. Rep.* **5**, 9006 (2015).
31. Mo, Y., Ong, S. P. & Ceder, G. Insights into diffusion mechanisms in P2 layered oxide materials by first-principles calculations. *Chem. Mater.* **26**, 5208–5214 (2014).
32. Lesnyak, V., Brescia, R., Messina, G. C. & Manna, L. Cu vacancies boost cation exchange reactions in copper selenide nanocrystals. *J. Am. Chem. Soc.* **137**, 9315–9323 (2015).
33. Groeneveld, E. et al. Tailoring ZnSe–CdSe colloidal quantum dots via cation exchange: from core/shell to alloy nanocrystals. *ACS Nano* **7**, 7913–7930 (2013).
34. Casavola, M. et al. Anisotropic cation exchange in PbSe/CdSe core/shell nanocrystals of different geometry. *Chem. Mater.* **24**, 294–302 (2012).
35. Takahashi, Y. et al. Anisotropic electrical conductivity in $LiCoO_2$ single crystal. *J. Solid State Chem.* **164**, 1–4 (2002).
36. Hill, G. T., Shi, F., Zhou, H., Han, Y. & Liu, C. Layer spacing gradient $(NaLi)_{1-x}CoO_2$ for electrochemical Li extraction. *Matter* **4**, 1611–1624 (2021).
37. Xue, Z. et al. Sodium doping to enhance electrochemical performance of overlithiated oxide cathode materials for Li-ion batteries via Li/Na ion-exchange method. *ACS Appl. Mater. Interfaces* **10**, 27141–27149 (2018).

Methods

Sample preparation

P3-$Na_{0.67}CoO_2$ and P2-$Na_{0.67}CoO_2$ were synthesized via the typical solid state method[38]. Na_2O_2 (Alfa, 95%) and Co_3O_4 (Alfa, 99.7%) were mixed in a Na:Co stoichiometric ratio of 0.68:1 (a slight excess Na) in an Ar glovebox. Thirty minutes of high-energy ball-milling was performed before pressing the mixture into a pellet. The transferring step from the ball-milling container to the press dies was finished in the Ar glovebox as well to minimize air contact. The pellet was heated at 535 °C for 16 h to obtain P3-$Na_{0.67}CoO_2$ and at 700 °C for 16 h to obtain P2-$Na_{0.67}CoO_2$. After cooling down to ~300 °C, the pellet was transferred into the Ar glovebox and stored for later use. Electrode slurries were prepared by mixing the active material, conductive carbon (Super P, MTI), and binder (polyvinylidene fluoride, MTI) in an 8:1:1 weight ratio, together with *N*-methyl-2-pyrrolidone (Sigma-Aldrich). The mass loading is ~2–3 mg active material per electrode. Electrodes were made by coating slurries on a carbon cloth substrate.

Electrochemical testing

All the electrochemical tests, including ion exchange with OCV recording and electrochemically assisted ion exchange, were conducted in a three-electrode system using an SP-300 potentiostat (BioLogic) in an Ar glovebox. Commercial non-aqueous Ag^+/Ag was used as the reference electrode (CH Instrument). Electrolytes were prepared by dissolving $LiClO_4$ and/or $NaClO_4$ in ACN to different ratios.

C/80 was used for collecting the galvanostatic curves of O3-Li_xCoO_2 using $LiCoO_2$ as the starting state (1 M Li ACN, $FePO_4$ as the counter electrode), P3-Na_yCoO_2 using $Na_{0.67}CoO_2$ as the starting state (1 M Na ACN, $FePO_4$ as the counter electrode during charging and $NaFePO_4$ as the counter electrode during the discharging) and P2-Na_yCoO_2 using $Na_{0.67}CoO_2$ as the starting state (1 M Na ACN, $FePO_4$ as the counter electrode during charging).

For ion exchange tests with OCV recording (starting material: Na parent electrode), Na_yCoO_2 with varying y was prepared via intercalation or deintercalation from the starting material $Na_{0.67}CoO_2$ in 30 ml 1 M Na ACN at C/40 with the counter electrode of $NaFePO_4$ (for $y = 0.77$ and 0.87) or $FePO_4$ (for $y = 0.37$, 0.47, and 0.57). After obtaining Na_yCoO_2 with target y, ion exchange experiments were conducted in 30 ml Li–Na ACN solutions (the Na concentration is fixed as 1 M if involved, and Li concentrations vary on the basis of the Li/Na ratio. $NaFePO_4$ was used as the counter electrode for 1–1,000, 1–100 and 1–10 Li/Na molar ratio solutions, and $LiFePO_4$ was used as the counter electrode for 1–1 and 1 M Li solutions.

For reversed ion exchange tests with OCV recording (starting material: Li parent electrode), commercial $LiCoO_2$ electrodes were deintercalated to Li_xCoO_2 ($x = 0.60$, 0.50 and 0.40) in 30 ml 1–1,000 Li/Na molar ratio (1 mM Li and 1 M Na) ACN solutions at C/10 with 41 h, 40 h and 39 h of further soaking in the same electrolyte, respectively. The counter electrode was $FePO_4$.

The electrochemically assisted ion exchange experiments were conducted in 30 ml 1–1,000 Li/Na molar ratio (1 mM Li and 1 M Na) ACN solution. The starting material is $Na_{0.67}CoO_2$. The counter electrode is $NaFePO_4$. The intercalation current in Fig. 4a is C/10. Additionally, 500 ml 1–10,000 Li/Na molar ratio ACN was used for further validating the electrochemically assisted ion exchange method (Supplementary Fig. 20).

The commercial $LiCoO_2$ was used for the potential calibration of the non-aqueous Ag^+/Ag reference electrode. The potential of the commercial $LiCoO_2$ is around 3.9 V versus Li^+/Li (−3.04 V versus standard hydrogen electrode) and is around 0.6 V versus the non-aqueous Ag^+/Ag reference electrode in 1 M Li ACN. Therefore, the potential of the non-aqueous Ag^+/Ag reference electrode is around 3.0 V versus Na^+/Na (−2.7 V versus standard hydrogen electrode). For better comparison, all the measured electrochemical curves were manually shifted by 3.0 V with Na^+/Na as the plotting reference point.

Figure Reading

In Fig. 4b, first, the grey lines were drawn as the guidelines assuming hypothetical ion exchange processes starting from Na_yCoO_2 to the final two-phase equilibrium of $Li_{0.94}CoO_2$ and $Na_{0.48}CoO_2$. The grey numbers on the left are the overall cation content ($a + b = A$ in $Li_aNa_bCoO_2$, equivalent to $1 - \upsilon$, the vacancy level). The calculation uses the evolution equation and assumes no kinetic barriers. Second, the empty circles were drawn on the basis of the calculation using the evolution equation at the specified vacancy levels (υ) and specified Na phases (Na components of Na phase, y, as x axis). For the empty red circles, they are from the intercalation process. The vacancy level (υ) was changed by the intercalation time, and the Na component in the Na phase (y) was obtained from the voltage. Then, the phase fraction (f) and Li content (a) were calculated. For the empty blue circles, they are calculated for each ion exchange process with the unchanged vacancy levels. Third, the ICP-MS measured compositions were drawn as the solid dots. Parallel electrochemically assisted ion exchange experiments are conducted and stopped at state I (2.87 V, refers to $Na_{0.64}CoO_2$), state II (3.10 V, refers to $Na_{0.565}CoO_2$), state IV (3.25 V refers to $Na_{0.50}CoO_2$) (Fig. 1b) and b, d, f and h (Fig. 4a), respectively.

$Li_{0.94}CoO_2$ and $Na_{0.48}CoO_2$ phase assignment

The newly appeared Li peak position matched well with $Li_{0.94\text{-}1.0}CoO_2$ (ref. 39). Considering the low electronic conductivity of Li_xCoO_2 at $0.94 \le x \le 1$ (refs. 39,40), which will induce a high energy barrier for Li insertion during ion exchange in a low Li/Na ratio solution, the newly appeared Li phase was assigned to $Li_{0.94}CoO_2$ instead of $Li_{1.0}CoO_2$. The new Na phase has an interlayer distance of 5.55 Å, which corresponds to Na_yCoO_2 at $0.3 < y < 0.5$ (ref. 41). The galvanostatic curve (Fig. 1a) gives $y = 0.48$ based on the final voltage, which was also confirmed by ICP-MS.

Equilibrium equation and evolution equation

$$(1 - x)f + (1 - y)(1 - f) = \upsilon,$$

where x is the Li component in the Li phase Li_xCoO_2, $x = 0.94$ at the equilibrium condition and during evolution; y is the Na component in the Na phase Na_yCoO_2, $y = 0.48$ at the equilibrium condition and $0.48 < y < 0.67$ during evolution; f is the phase fraction of the Li phase; υ is the total vacancy in the structure ($1 - \upsilon = a + b$). The Li content, a, and Na content, b, in the two-phase mixture with an overall composition of $Li_aNa_bCoO_2$ (a and b are different from x and y in the Li and Na phases) after reaching equilibrium can be calculated by $a = x \times f$ and $b = y \times (1 - f)$. During evolution, Na components y ($y = 0.64$, 0.565 and 0.50 at plateaus I, II and IV, respectively) are determined by comparing the plateau voltages of OCV curves and that of the galvanostatic curve (Fig. 1a).

Structural selectivity

The structural selectivity is calculated on the basis of the final composition $Li_aNa_bCoO_2$ versus the Li/Na ratio in the system as (a/b)/ratio.

The calculation of the excess amount of Li

The Li amount provided in 30 ml 1–1,000 Li/Na molar ratio ACN solution is 0.03 mmol. The exchanged Li amount in the 3 mg electrode with a final composition of $Li_{0.90}Na_{0.02}CoO_2$ is 0.0254 mmol. The excess amount of Li is calculated as 18%.

XRD

Synchrotron XRD measurements (0.1173 Å) were conducted at the 13-BM beamline of the Advanced Photon Source. The intensities in Fig. 1c and Fig. 2b have been normalized to make the strongest diffraction peaks have the same intensity. XRDs of P2-Na_2CoO_2, converted $Li_{0.90}Na_{0.02}CoO_2$ and converted Na_yCoO_2 were collected by using Rigaku

MiniFlex 600 with a Cu Kα source. The Rietveld refinements were carried out using GSAS II. The instrument parameters were modified on the basis of the 'defaults for APS 30KeV 11BM'. Diffractions of single-phase $Na_{0.57}CoO_2$ and $Na_{0.67}CoO_2$ were first refined on the basis of literature[41,42]. The unit cell and atom coordination were refined. The obtained phase information as the reference was used for refining biphasic diffractions. Phase fraction was added for the biphasic diffraction refinement.

STEM

The top view of equilibrium particles showing Li–Na phase separation and atomic-resolution images of the fully converted $Li_{0.90}Na_{0.02}CoO_2$ were obtained by using the aberration-corrected scanning transmission electron microscope JEOL ARM200CF (200 kV) at the University of Illinois at Chicago. The HAADF detector angle was 90–270 mrad to give *Z* contrast images. The low-angle annular dark-field detector angle ranged between 40 and 120 mrad. The energy dispersion for EELS (Gatan) was 0.15 eV per pixel with 0.1 s per pixel dwell time. EDS spectrum imaging was performed using an Oxford X-Max 100TLE windowless SDD detector. The cross-section view of the fully converted $Na_{0.48}CoO_2$ was obtained using the aberration-corrected scanning transmission electron microscope JEOL ARM200CF (200 kV) at Northwestern University. EDS spectrum imaging was performed using a Dual SDD EDS detector.

Particles were removed from the electrodes after reaching the equilibrium by sonication in *N*-methyl-2-pyrrolidone and were drop-cast onto lacey carbon membrane-coated gold grids for top view imaging. For the cross-section view imaging of the converted $Li_{0.90}Na_{0.02}CoO_2$, particles were embedded into Poly/Bed 812 resin after removing from the electrodes and cut into 90-nm-thick slides using a ultramicrotome (Ultracut E, Reichert-Jung). For the cross-section view imaging of the converted $Na_{0.48}CoO_2$, micrometre-sized particles were removed from the electrodes, which were site-specifically cut and thinned using conventional focused ion beam-SEM (FEI Helios NanoLab 600). Specifically, a ~150-nm-thick carbon layer and ~1.2-μm-thick platinum layer were initially deposited using a gas injection system to protect the surface of the target particle. After removal of an approximately 8 × 2 × 4 μm section via in situ lift-out using a W micromanipulator (Oxford Omniprobe 200), the lamella was thinned at initially 30 kV, 0.49 nA and subsequently at 5 kV, 81 pA. Finally, the sample was cleaned at 2 kV and 28 pA to yield a ~90-nm-thick lamella.

SEM

Scanning electron micrographs were obtained on a Zeiss Merlin scanning electron microscope using a 20 kV accelerating voltage. EDS spectra imaging was acquired using an Oxford Ultim Max 100 EDS detector.

ICP-MS

As the diluting matrix, 3% HNO_3(aq) was used, and all the measurements used either Thermo iCAP Q ICP-MS or Thermo iCAP RQ ICP-MS.

Before dissolving, each electrode was washed at least six times, each time with 10 ml ACN solution to remove residual salts on the surface as completely as possible. Eight millilitres of aqua regia was used to dissolve each electrode.

DFT calculation

A 2 × 2 × 2 supercell based on the rhombohedral primitive cell of P3-$NaCoO_2$ was used to explore the different Na/Li/vacancy configurations in the region of $0 \le a + b \le 1$ with a step size of 0.125. We used the Pymatgen[43] software package to enumerate the orderings by replacing Na sites with vacancy or lithium. We also applied similar approach on a 3 × 3 × 1 supercell to explore the composition line of $Na_{2/3-a}Li_aCoO_2$. We use the Vienna ab initio simulation package[44–46] (VASP) to perform DFT calculations to relax the lattice and atomic position and calculate the final energies of these structures. The exchange and correlation energy were integrated on a 25 $Å^{-1}$**k** point mesh, calculated using the Perdew–Burke–Ernzerhof spin-polarized generalized gradient approximation[47]. The energy is converged within 10^{-5} eV per cell, and the atomic forces were converged within 0.01 eV $Å^{-1}$. We also consider the Coulomb correlation of 3*d* electrons of cobalt by introducing 3.4 eV of Hubbard's *U* correction[48,49].

The interface models of $LiCoO_2$–$Na_{0.5}CoO_2$ and $Li_{2/3}CoO_2$–$Na_{2/3}CoO_2$ were built on the basis of the most stable ordering from both our calculation and reported results[50]. For the $LiCoO_2$–$Na_{0.5}CoO_2$ interface, we built a supercell with 72 formula units based on the primitive cell of P3-$NaCoO_2$, then applied the Na orderings on half of the supercell and Li ordering on the rest of the supercell. For $Li_{2/3}CoO_2$–$Na_{2/3}CoO_2$, the supercell contains 54 formula units. The interlayer distance at the interface is set to 5.1 Å. The interface model is fully relaxed using DFT calculation. The interfacial energy, defined as the energy difference between the interface model and bulk structure of A and B, is calculated by

$$\sigma = \frac{1}{2S}\left(E_{\text{int}} - N_A E_A - N_B E_B\right),$$

where E_{int} is the DFT total energy of interface model that contains N_A and N_B formula units of structures A and B, respectively, in the interface model. *S* is the surface area of interface model, and E_A and E_B are the energy per formula unit of structures A and B, respectively.

Data availability

The authors declare that all relevant data are included in the paper and Supplementary Information files and are available from the corresponding author upon reasonable request.

References

38. Lei, Y., Li, X., Liu, L. & Ceder, G. Synthesis and stoichiometry of different layered sodium cobalt oxides. *Chem. Mater.* **26**, 5288–5296 (2014).
39. Ménétrier, M., Saadoune, I., Levasseur, S. & Delmas, C. The insulator–metal transition upon lithium deintercalation from $LiCoO_2$: electronic properties and 7Li NMR study. *J. Mater. Chem.* **9**, 1135–1140 (1999).
40. Dahéron, L. et al. Electron transfer mechanisms upon lithium deintercalation from $LiCoO_2$ to CoO_2 investigated by XPS. *Chem. Mater.* **20**, 583–590 (2008).
41. Viciu, L. et al. Crystal structure and elementary properties of Na_xCoO2 (x=0.32, 0.51, 0.6, 0.75, and 0.92) in the three-layer $NaCoO_2$ family. *Phys. Rev. B* **73**, 174104 (2006).
42. Ono, Y. et al. Crystal structure, electric and magnetic properties of layered cobaltite β-Na_xCoO_2. *J. Solid State Chem.* **166**, 177–181 (2002).
43. Ong, S. P. et al. Python Materials Genomics (pymatgen): a robust, open-source Python library for materials analysis. *Comput. Mater. Sci.* **68**, 314–319 (2013).
44. Kresse, G. & Hafner, J. Ab initio molecular dynamics for liquid metals. *Phys. Rev. B* **47**, 558–561 (1993).
45. Kresse, G. & Furthmüller, J. Efficient iterative schemes for ab initio total-energy calculations using a plane-wave basis set. *Phys. Rev. B* **54**, 11169–11186 (1996).
46. Kresse, G. & Joubert, D. From ultrasoft pseudopotentials to the projector augmented-wave method. *Phys. Rev. B* **59**, 1758–1775 (1999).
47. Perdew, J. P., Burke, K. & Ernzerhof, M. Generalized gradient approximation made simple. *Phys. Rev. Lett.* **77**, 3865–3868 (1996).
48. Cococcioni, M. & de Gironcoli, S. Linear response approach to the calculation of the effective interaction parameters in the LDA+U method. *Phys. Rev. B* **71**, 035105 (2005).

49. Dudarev, S. L., Botton, G. A., Savrasov, S. Y., Humphreys, C. J. & Sutton, A. P. Electron-energy-loss spectra and the structural stability of nickel oxide: an LSDA+U study. *Phys. Rev. B* **57**, 1505–1509 (1998).
50. Kaufman, J. L. & Van Der Ven, A. Na_xCoO_2 phase stability and hierarchical orderings in the O3/P3 structure family. *Phys. Rev. Mater.* **3**, 015402 (2019).

Acknowledgements

We thank Y. Chen for performing ultramicrotome cutting. This work is supported by the US Department of Energy (DOE), Office of Basic Energy Sciences under award DE-SC0022231. This research used resources of the Advanced Photon Source, a US DOE Office of Science user facility operated for the DOE Office of Science by Argonne National Laboratory under contract DE-AC02-06CH11357. This work made use of instruments in the Electron Microscopy Core of UIC's Research Resources Center. Acquisition of UIC JEOL ARM200CF was supported by a MRI-R2 grant from the National Science Foundation (DMR-0959470). The Gatan Continuum GIF acquisition at UIC was supported by a MRI grant from the National Science Foundation (DMR-1626056). This work made use of the EPIC facility of Northwestern University's NUANCE Center, which has received support from the SHyNE Resource (NSF ECCS-2025633), the IIN and Northwestern's MRSEC programme (NSF DMR-1720139). P.C. acknowledges funding from the National Research Foundation under NRF Fellowship NRFF12-2020-0012. We acknowledge that the computational work involved in this research is supported by National University of Singapore IT Research computing group (https://nusit.nus.edu.sg), and we thank software tuning support from M. Dias Costa and W. Junhong. This work used computational resources of the supercomputer Fugaku provided by RIKEN through the HPCI System Research Project (project ID hp 230188). A proportion of computational work was performed on resources of the National Supercomputing Centre, Singapore (https://www.nscc.sg).

Author contributions

C.L. and Y.H. conceived and developed the idea and planned the experiments. P.C. and W.X. performed the DFT calculation. G.T.H., H.Z. and S.Z. performed the synchrotron XRD measurement. P.S., X.H. and Y.H. performed the STEM imaging, EELS and EDS analysis with the assistance of F.S. G.Y. assisted with the ICP-MS data acquirement. S.Z. performed the SEM imaging. J.L. and R.W. helped with data collation during revision. All authors analysed the data and co-wrote the paper.

Competing interests

The authors declare no competing interests.

Additional information

Supplementary information The online version contains supplementary material available at https://doi.org/10.1038/s41563-024-01862-8.

Correspondence and requests for materials should be addressed to Chong Liu.

Peer review information *Nature Materials* thanks the anonymous reviewers for their contribution to the peer review of this work.